Supplementary

Highly sensitive/selective 3D nanostructured immunoparticle-based interface on a multichannel sensor array for detecting amyloid-beta in Alzheimer's disease

Ta-Chung Liu[a], Yi-Chao Lee[b], Chiung-Yuan Ko[b], Ren-Shyan Liu[c,d], Chien-Chih Ke[c,d], Yu-Chun Lo[b], Pei-Sung Hong[a], Chao-Yi Chu[a], Ching-Wen Chang[e], Pu-Wei Wu[a], You-Yin Chen[b,e,*], and San-Yuan Chen [a,f,*]

[a]Department of Materials Science & Engineering, National Chiao Tung University, No. 1001, Ta-Hsueh Rd., Hsinchu, Taiwan 30010, R.O.C.

[b]The Ph.D. Program for Neural Regenerative Medicine, Taipei Medical University, No. 250 Wu-Xing St., Taipei 11010, Taiwan, R.O.C.

[c]Department of Biomedical Imaging and Radiological Sciences, National Yang Ming University, No.155, Sec.2, Linong St., Taipei, Taiwan 11221, R.O.C.

[d]Department of Nuclear Medicine and National PET/Cyclotron Center, Taipei Veterans General Hospital, No.201, Sec. 2, Shipai Rd., Taipei, Taiwan 11217, R.O.C.

[e]Department of Biomedical Engineering, National Yang Ming University, No.155, Sec.2, Linong St., Taipei, Taiwan 11221, R.O.C.

[f]Frontier Research Center on Fundamental and Applied Sciences of Matters, National Tsing Hua University, Taiwan 30010, R.O.C.

[*]Correspondence should be addressed to either of the following:
You-Yin Chen, Department of Biomedical Engineering, National Yang Ming University, No.155, Sec.2, Linong St., Taipei, Taiwan 11221, R.O.C.
E-mail: irradiance@so-net.net.tw
San-Yuan Chen, Department of Materials Science and Engineering, National Chiao Tung University, No. 1001, Ta-Hsueh Rd., Hsinchu, Taiwan 30010, R.O.C.
Email: sanyuanchen@mail.nctu.edu.tw

Note 1. Fabrication of microelectrode immunosensor array (MEIA) and its specifications

AutoCAD (AutoCAD 2002, Autodesk Inc., USA) was used to plot the main elements of the MEIA chip: the integrated connector pads, 56 microelectrodes (MEs) for electrophysiological recording, and 4 reference electrodes (REs). The respective specifications are listed in **Table S1** and depicted in **Figure S1**.

Two masks were used in the fabrication process for the MEIA chip. The first mask (MASK #1) was used to create 60 electrodes (30 μm in diameter, 200 μm spacing), lead wires and corresponding connection pads at the edge of the MEIA. The second mask (MASK #2) was used to create the electrodes and connection pads.

The process was started by coating polyimide (PI-2611, HD Microsystems, Parlin, NJ, USA) at a thickness of 60 μm onto the glass wafer with a spin coater (Model KW-4A, Chemat Technology Inc., Northridge, CA, USA) and curing the coated wafer at 350 °C for 30 min in an inert gas oven (QHMO-2, CSUN MFG. Ltd., New Taipei City, Taiwan). Chrome and copper, 100 nm and 700 nm in thickness, respectively, were sputtered onto the polyimide layer as a conduction layer by a reactor. MASK #1 was used to lithographically pattern the metal circuits, which included 60 electrodes, lead wires and connection pads. Chrome and copper were etched by chrome etchant (eSolv EG-201, Demand International Corp., Hsinchu, Taiwan) and copper etchant (RTE-Cu29 WBL-B, Resound Technology Inc., Kaohsiung, Taiwan), respectively, to create the circuit. Negative photosensitive polyimide was spin-coated to form an insulation layer with a thickness of 3.2 μm. MASK #2 was used to lithographically pattern the electrodes and connection pads.

To achieve a three-dimensional (3D) structure of electrodes and connection pads, an electroplating technique was applied. Optimal electroplating parameters and control procedures were used to refine the structure of the electrodes and the connector pads of the deposition. The 5-μm-thick gold layer was deposited

at the electrode sites and connection pads. Finally, a glass ring (inner diameter = 22 mm, outer diameter = 25 mm, height = 10 mm) was attached to the center of the glass plate by a silicon adhesive (SYLGARD® 184 Silicone elastomer kit, Dow Corning Corp., Midland, MI, USA) to construct a culture chamber. The process diagram is illustrated in **Figure S2**.

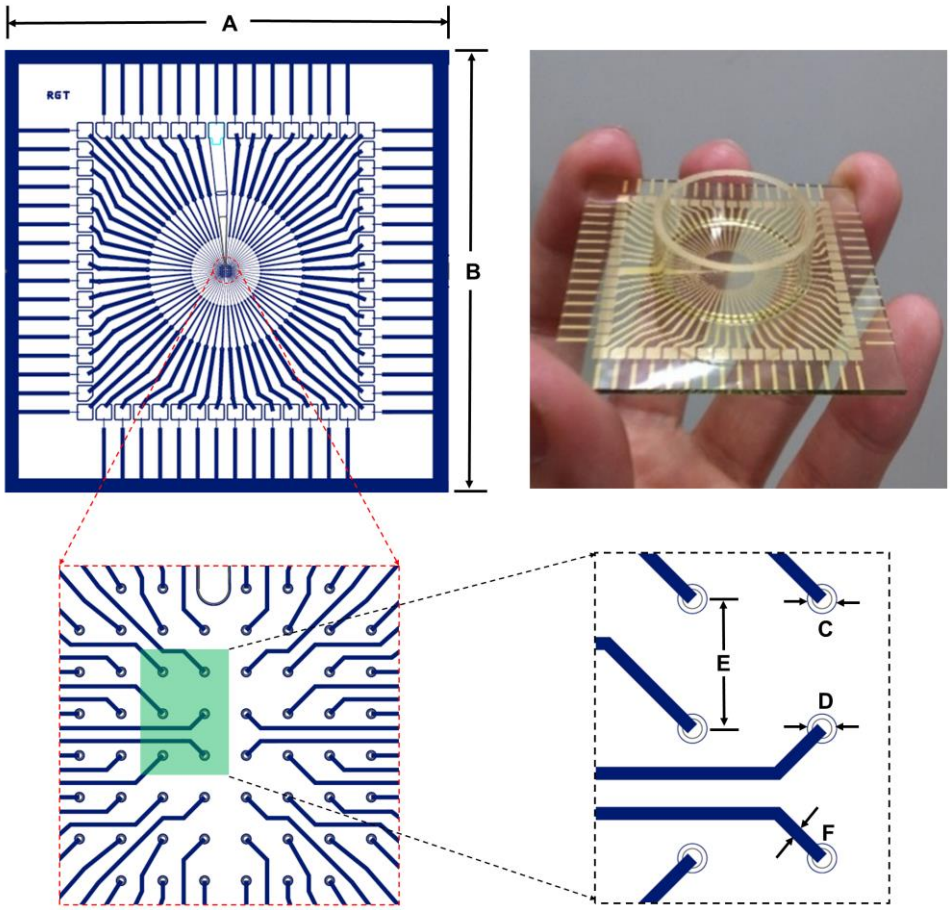

Figure S1. Schematic layout of the microelectrode immunosensor array (MEIA) chip depicted by AutoCAD (not drawn to scale) and an overview image of the MEIA chip. The chip includes 56 microelectrodes (MEs), and 4 reference electrodes (REs). Connector pads corresponding to REs are highlighted in blue. See **Table S1** for detailed dimensions.

Table S1. Specifications of the MEIA chip.

Parameter	Value
Number of MEs	56
Number of REs	4
Number of pads	60
Length of Chip (**A**) (cm)	5.7
Width of Chip (**B**) (cm)	5.7
ME radius (**C**) (μm)	60
RE radius (**D**) (μm)	60
Distance of ME interspace (**E**) (μm)	200
Width of wire (**F**) (μm)	30

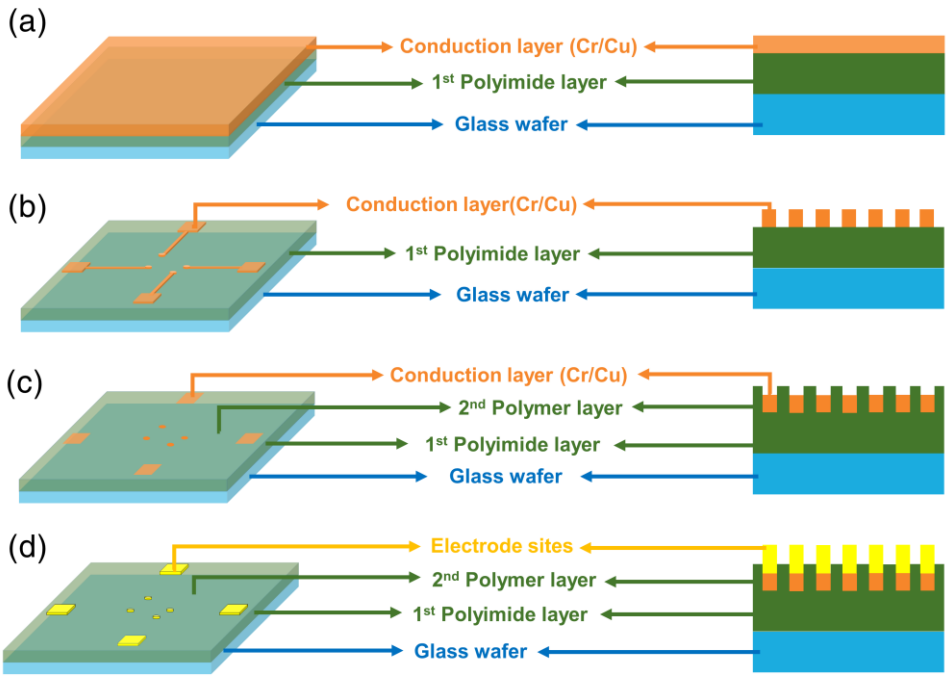

Figure S2. A schematic illustration of the fabrication process for the MEIA chip (not drawn to scale). (a) The conductive layer was deposited over the first 60-μm thick polyimide layer. (b) The metallic layer was patterned upon the 1st polyimide layer, which was then etched to construct the 60 electrodes/connector pads and interconnect tracks. (c) The protective polyimide layer (3.2 μm) was spun onto the conduction layer; the 60 electrodes/connector pads were deprotected. (d) Gold was electroplated to form 56 microelectrodes (MEs) and 4 reference electrodes (REs).

Note 2. ROI definition

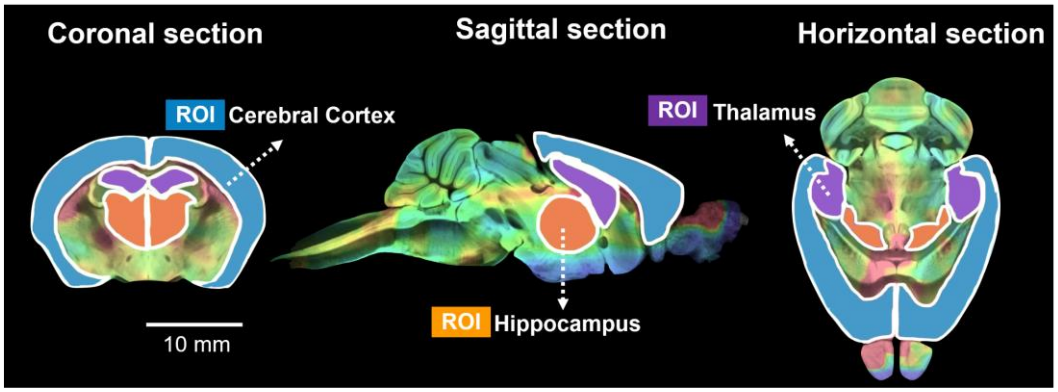

Figure S3. Three regions of interest (ROIs) were used to determine [^{11}C]PiB specifically binding to Aβ plaques in bilateral cerebral cortices including primary somatosensory cortices (SI), secondary somatosensory cortices (SII), anterior cingulated cortices (ACC), agranular insular cortices (AIC), and primary/secondary motor cortices (MC) (blue), bilateral thalami (purple) and bilateral hippocampi (orange). ROIs were defined on horizontal, coronal and sagittal sections of the co-registered PET-MRI image of the mouse brain, and were aligned on the atlas to the matching structures on the brain images. Precise localization of ROIs was achieved.

Note 3. Phase diagram of EDOT in SF with different pH

Figure S4. The miscibility of amphiphilic silk fibroin and hydrophobic EDOT monomers was strongly dependent on the pH value at various EDOT doping concentrations. The silk fibroin solutions of pH were adjusted by preparing the buffer solution (S25208 A-k, Fisher Scientific Inc., Waltham, MA, USA) ranging from pH = 4 to pH = 10. At a higher pH, most charged amino acid side chains except the C-terminus are negatively charged, likely resulting in an elongated molecular conformation in solution due to repulsive charge-charge interactions along the biopolymer backbone. The EDOT doping concentration reached saturation in the silk fibroin matrix at pH > 9.

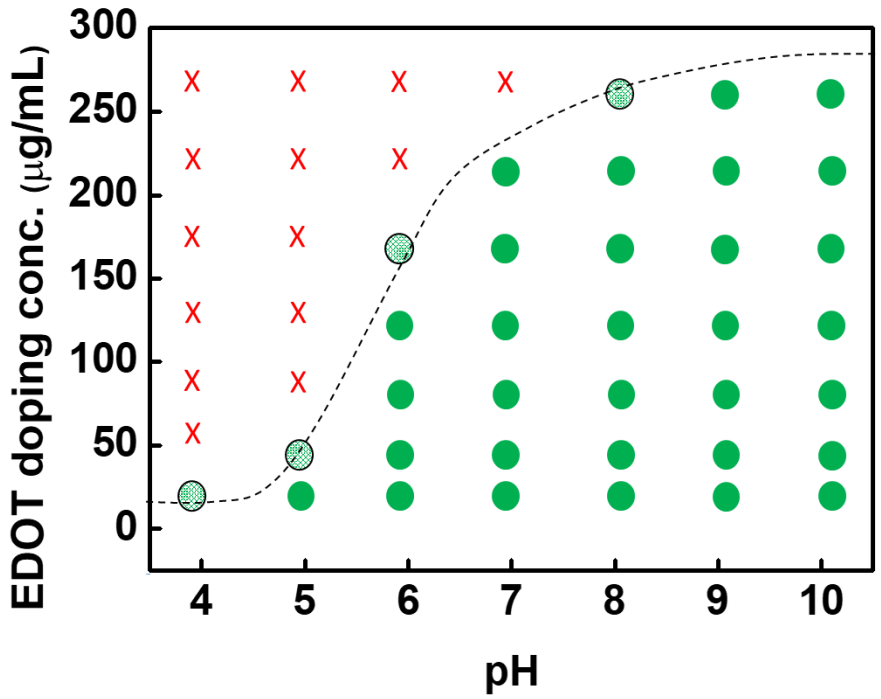

Figure S4. Phase diagram of the miscibility with different concentrations of EDOT as a function of pH in SF solutions.

Note 4. XPS spectrum of CSPs and CSIPs

XPS was used to characterize the surface chemistry of the Aβ antibodies bio-conjugation on CSPs. The high-resolution XPS in **Figure S5**(a)-(b)-B shows that characteristic chemical bonding of C-N, C=O, O=C-NH in C1s region and NH_2, CO-NH-C in N1s were all from silk fibroin. However, in **Figure S5**(c), C-N bonding was much stronger than any other bonding in C1s region, indicative of that the reactive aldehyde groups located in Fc binding of Aβ antibodies reacted with NH_2 of silk fibroin to form C-N conjugating through $NaIO_4$ activating. Furthermore, NH_2, which consumes reactive aldehyde groups of Aβ antibodies, was smaller compared with silk-based nanoparticles before antibodies conjugating in N1s region shown in **Figure S5**(d).

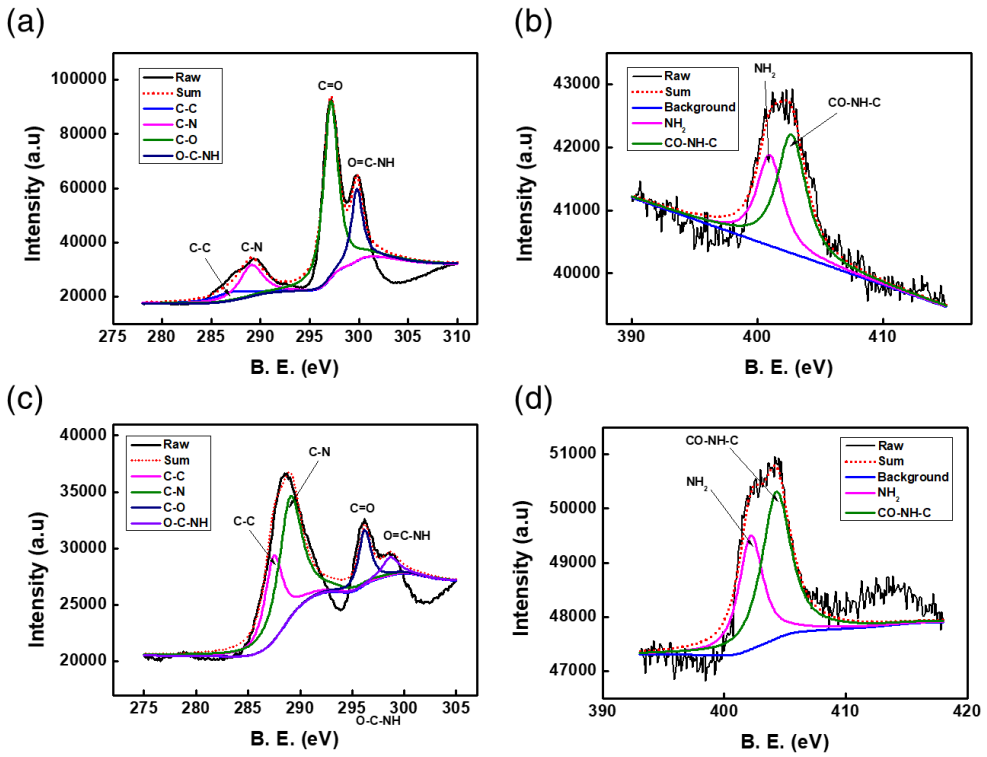

Figure S5. XPS data of (a) C1s region and (b) N1s region of CSPs. XPS data of (c) C1s region and (d) N1s region of CSIPs.

Note 5. Fabrication of the CSIP-modified microelectrode by CV

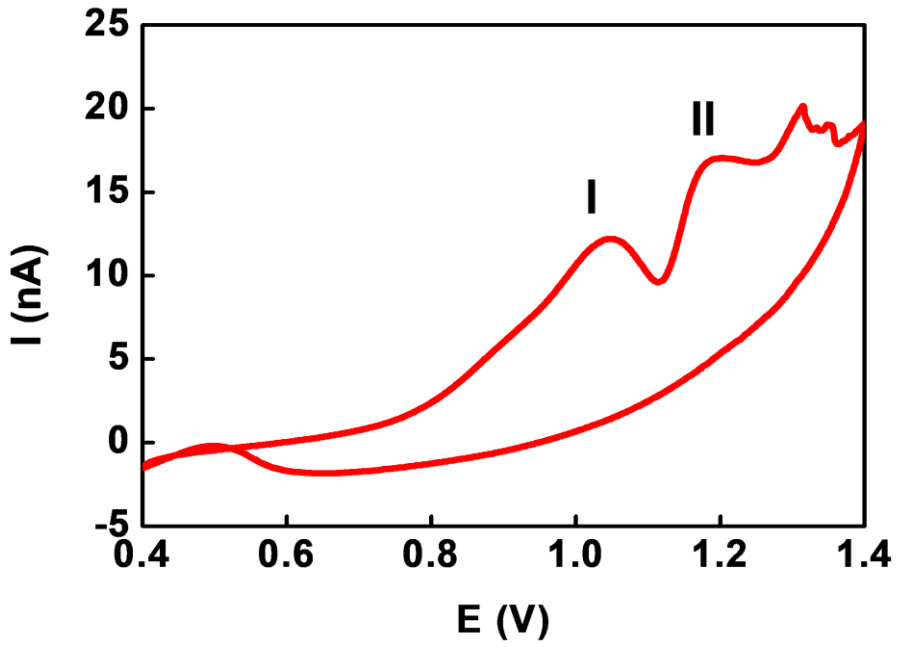

Figure S6. The real-time CV curve of one-step electrophoresis/electropolymerization of CSIP-modified microelectrodes on the MEIA platform.

Note 6. FTIR spectra of CSIPs, EDOT and SF

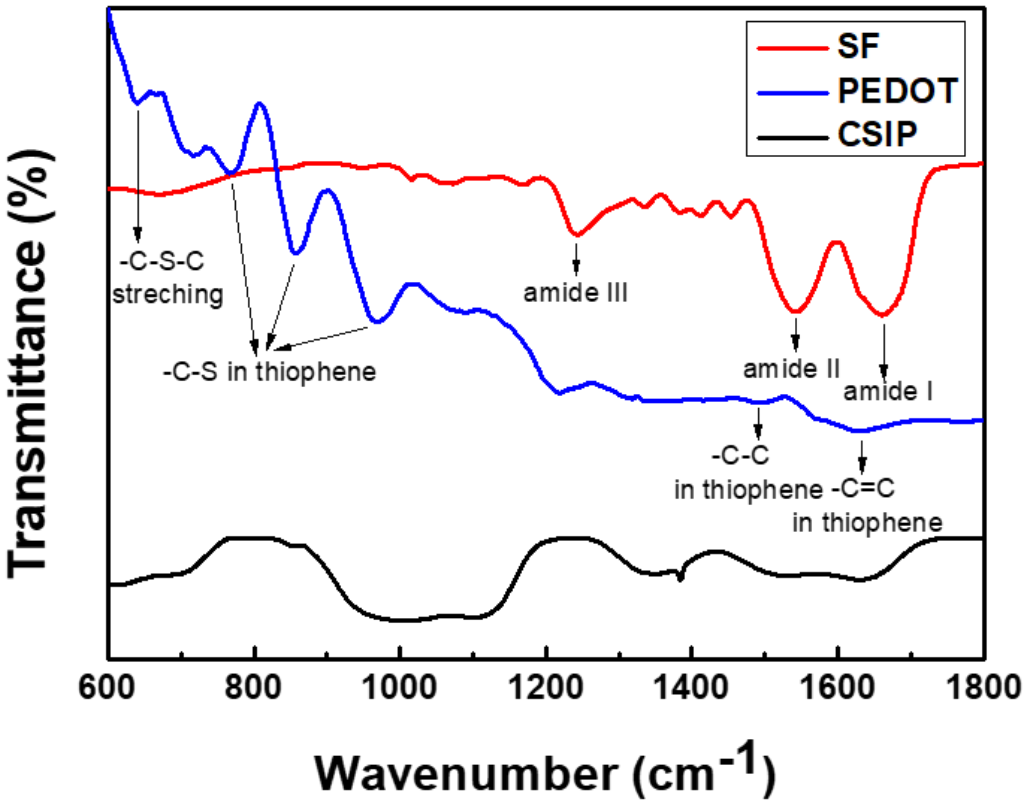

Figure S7. FTIR spectra of SF, PEDOT, and CSIP.

Note 7. Phase diagram of the EDOT doping in SF

Figure S8 shows the phase diagram describing the miscibility of hydrophobic EDOT monomers and amphiphilic SF. The boundary between the soluble phase and insoluble phase indicates a maximum EDOT doping in the SF matrix.

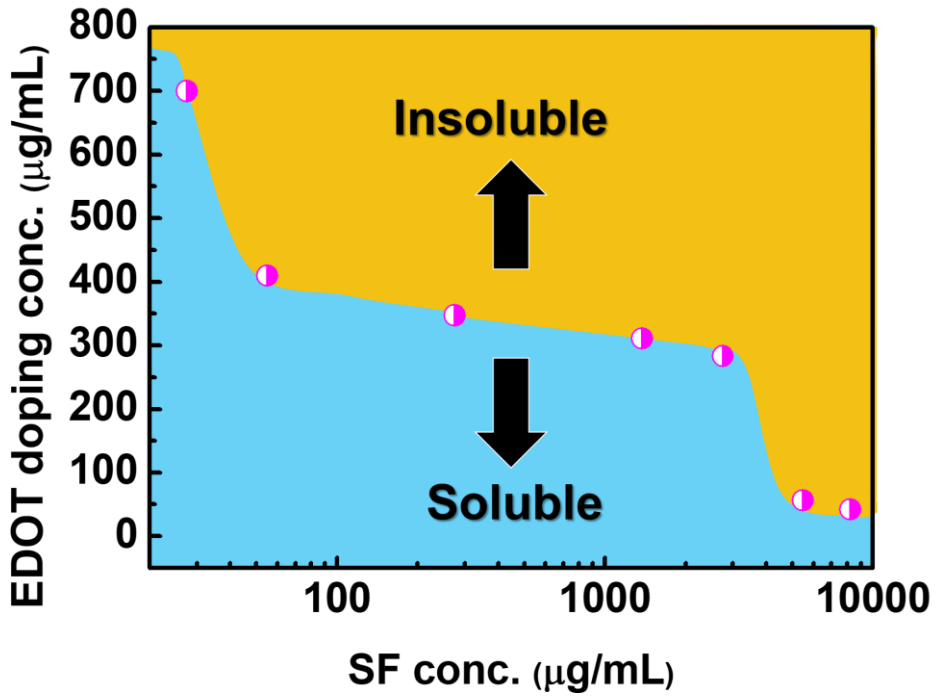

Figure S8. Phase diagram of the EDOT doping with different concentrations of silk fibroin (SF). Half-filled dots indicate the maximum EDOT doping amount in SF in the homogeneous state.

Note 8. Size distributions of CSIPs

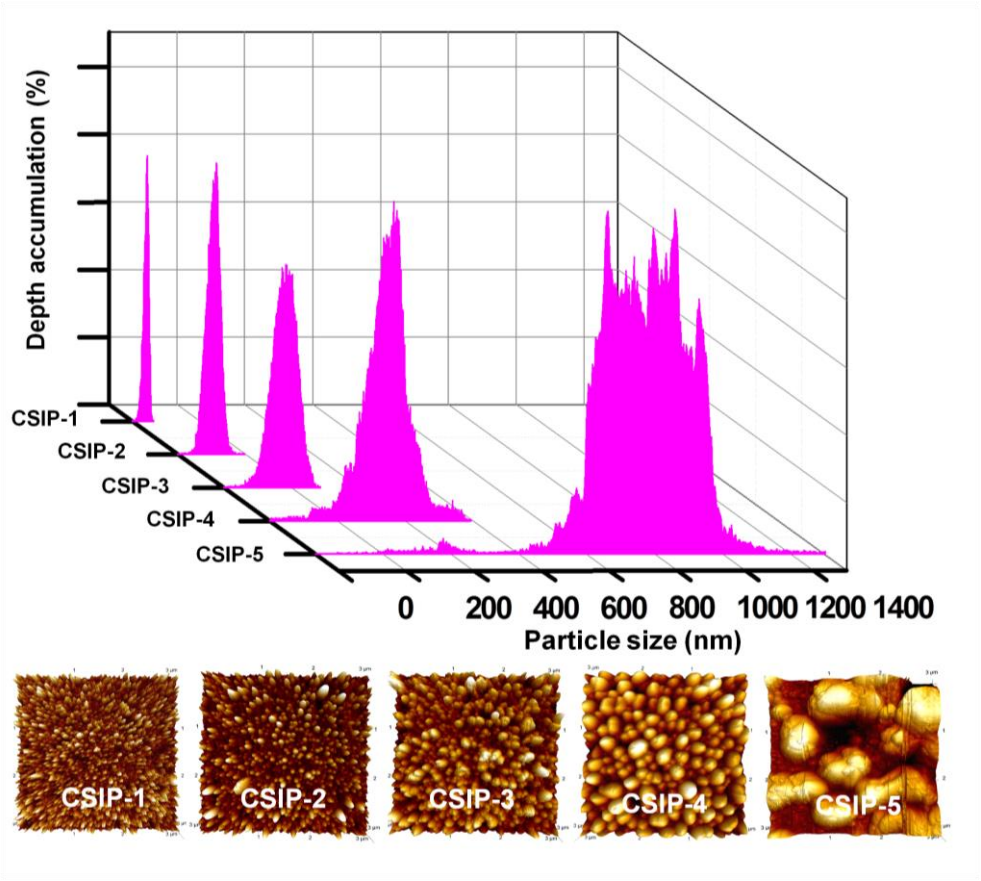

Figure S9. Size distribution of CSIP-1 to CSIP-5.

Table S2. The physical and chemical properties of CSIP-1 to CSIP-5 modified microelectrodes

Microelectrode	SF (mg/mL)	Particle size	ζ potential	R_{ct} (Ω)	Surface area
CSIP-1	0.0275	47 ±16.2	-25.6	62.5	
CSIP-2	0.055	91 ±28.1	-36.3	75.8	
CSIP-3	0.275	207 ±55.6	-41.5	194.2	
CSIP-4	1.375	311 ±24.0	-47.1	243.7	
CSIP-5	2.75	906 ±171.5	-51.1	3080.4	

Note 9. Cyclic voltammetry of CSIP-modified microelectrodes

The cyclic voltammatry (CV) of $CSIP_{40}$-1 to $CSIP_{40}$-5 (shown in **Figure S10**) was tested from -0.2 V to 0.8 V at a scan rate of 10 mV/s. The integration area of the CV curve for $CSIP_{40}$-1 modified microelectrode showed excellent ion/charge conductivity compared to other CSIP-modified microelectrodes; however, the $CSIP_{40}$-2 modified microelectrode performed higher redox peak currents than other modified microelectrodes due to its high antibody bindings. In sum, $CSIP_{40}$-2 modified microelectrode was used for proof-of-concept detection *in vitro* and *ex vivo*.

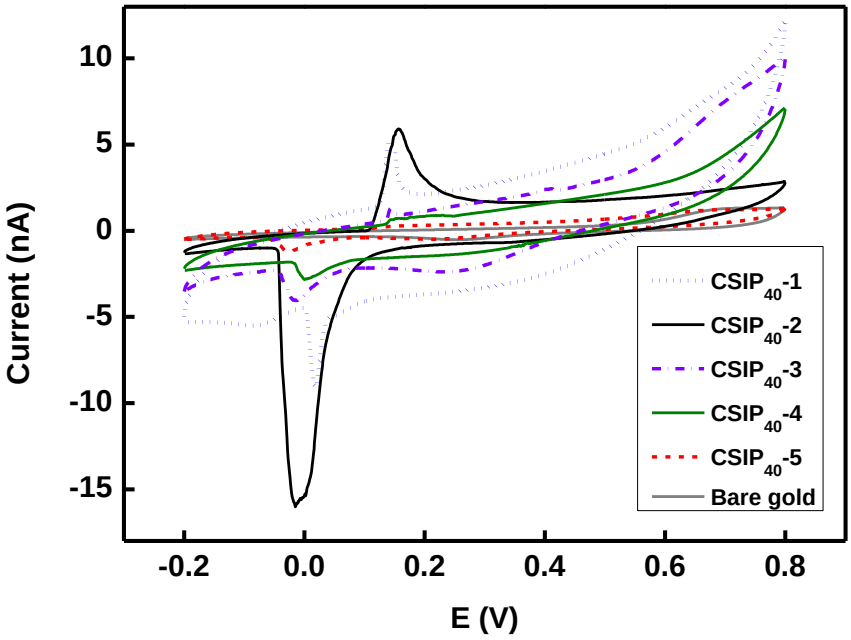

Figure S10. CVs recorded with $CSIP_{40}$-1 to $CSIP_{40}$-5 with 1 μg/mL $A\beta_{40}$ antibody coupling in 0.1M PBS at 10 mVs^{-1}.

Note 10. Comparisons of the detection limit of $CSIP_{40}$-1 to $CSIP_{40}$-5.

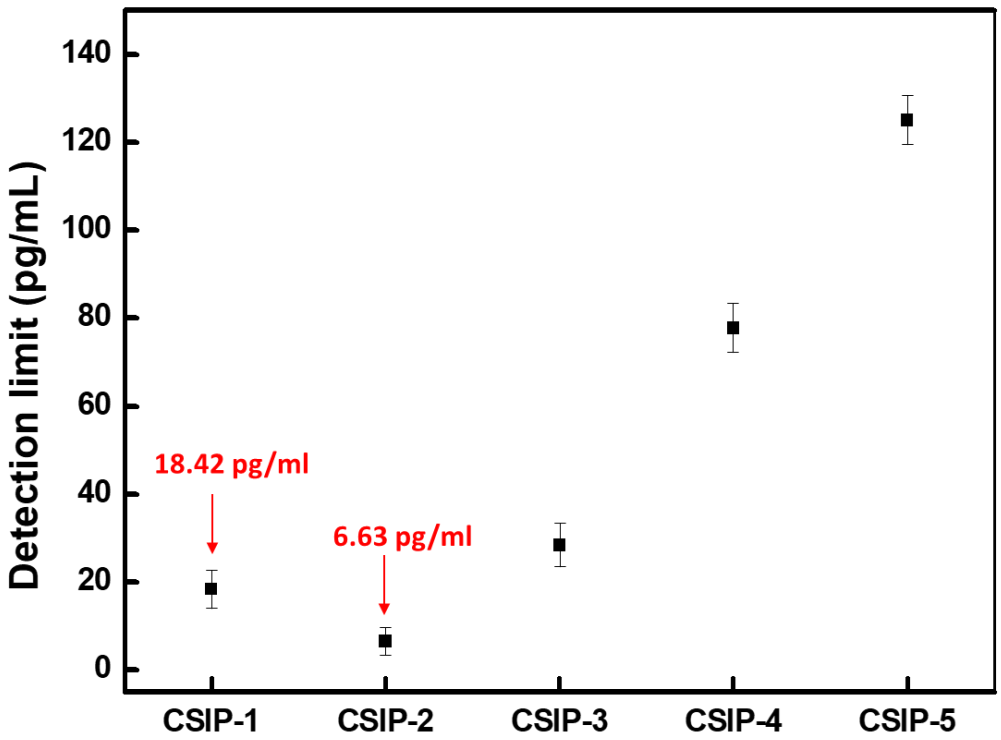

Figure S11. Comparisons of the detection limit of $CSIP_{40}$-1 to $CSIP_{40}$-5.

Note 11. Water contact angles of $PEDOT_{40}$, FSP_{40} and $CSIP_{40}$ modified electrodes

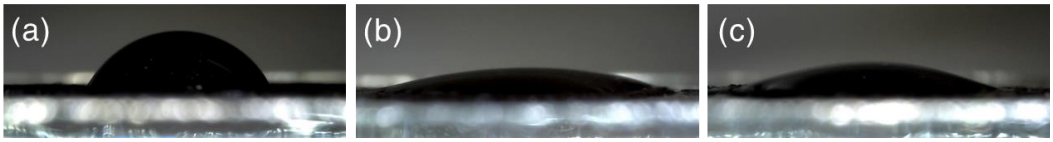

Figure S12. Water contact angles of 73.7°, 30.3° and 51.5° for (a) $PEDOT_{40}$, (b) FSP_{40} and (c) $CSIP_{40}$ modified electrodes, respectively.

Note 12. Evaluation of response time of MEIA platform

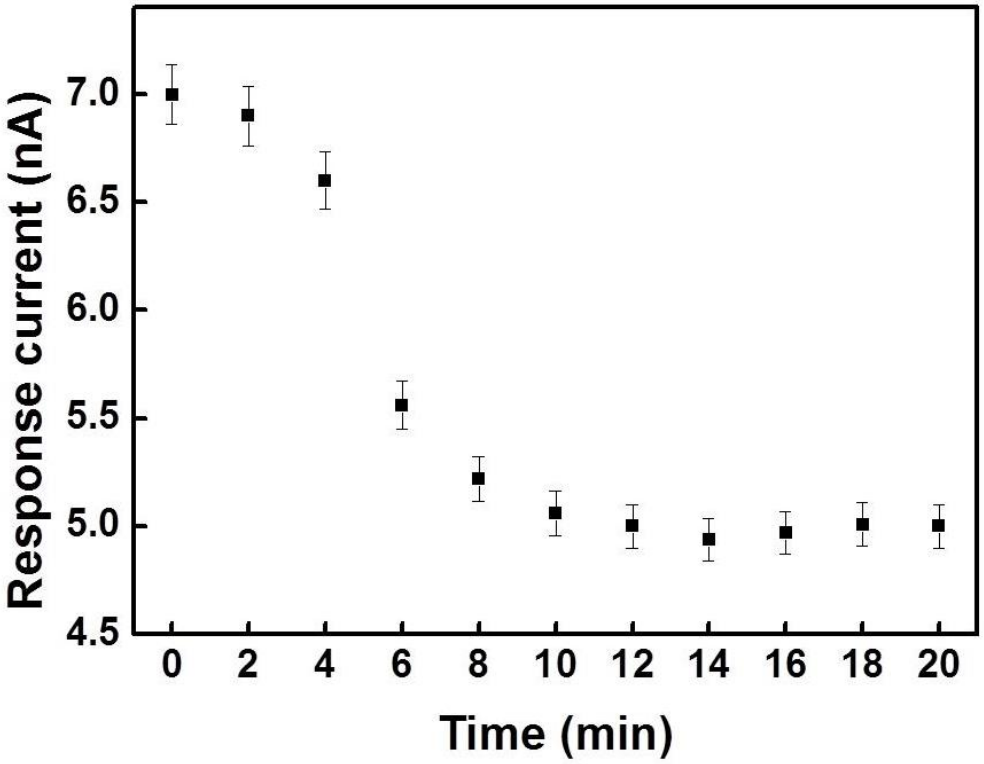

Figure S13. $CSIP_{40}$-2 modified microelectrode on MEIA platform incubated with 20 pM $A\beta_{40}$ solution. LSV was performed every 2 min using 10 mM PBS as the supporting electrolyte. The oxidation peak current was plotted versus responding incubation time.

Note 13. The stability of CSIP$_{40}$-2 and CSIP$_{42}$-2 modified microelectrode on the MEIA platform

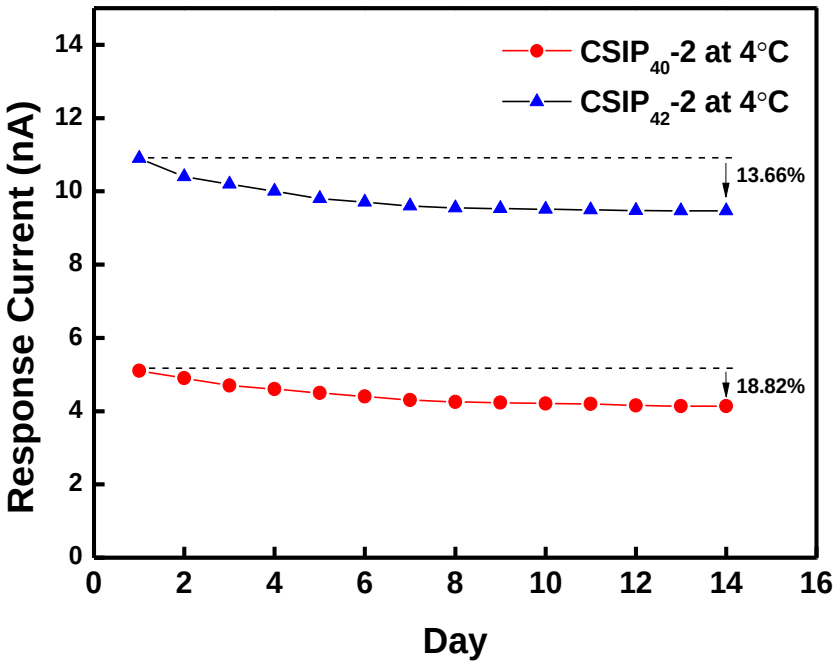

Figure S14. The stability of CSIP$_{40}$-2 and CSIP$_{42}$-2 microelectrodes.

Note 14. The evaluation of $A\beta_{42}$ over $A\beta_{40}$ ratio

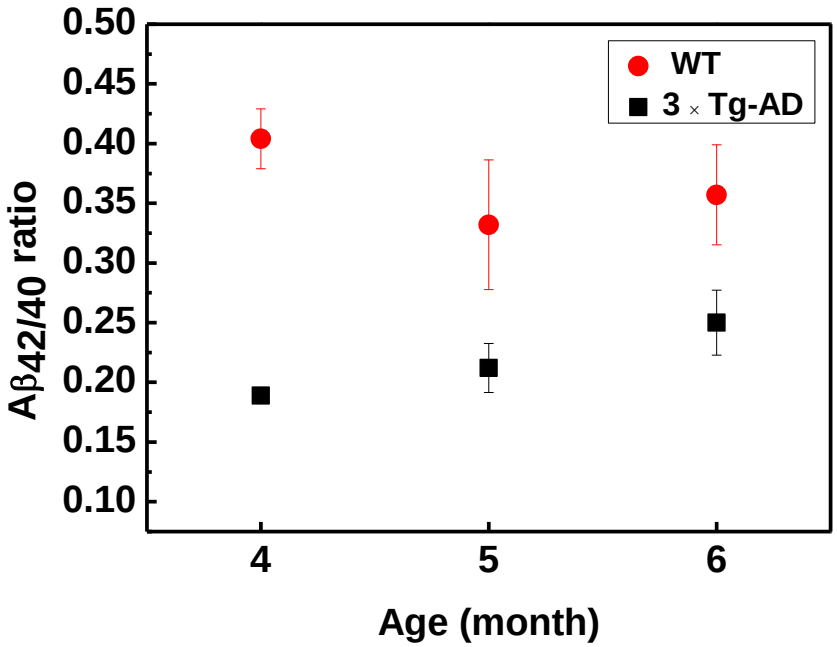

Figure S15. Relative ratio of $A\beta_{42}$ over $A\beta_{40}$ with age (n = 6 for each group).

Note 15. Comparison of PET imaging with [^{11}C]PiB in AD and WT mice

[^{11}C]PiB retention quantified Aβ plaque buildup as shown in **Figure S16**, and significant [^{11}C]PiB uptake in the cerebral cortex, hippocampus and thalamus was found from the age of 5 months to 6 months in AD mice. This Aβ plaque buildup indicated the onset and worsening of the brain with more prominent and severe AD phenotype [1].

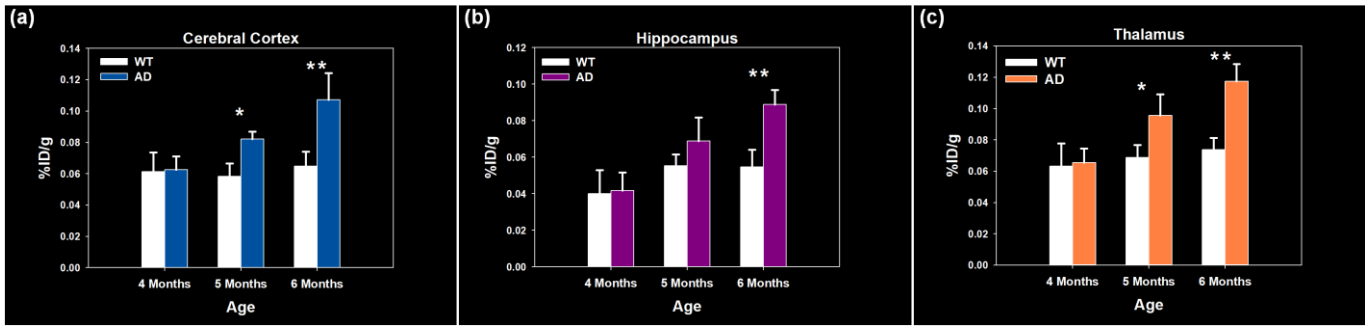

Figure S16. Comparison of [^{11}C]PiB uptakes in AD and WT mice. PET images acquired for 4-, 5- and 6-month-old AD mice and WT mice to compare [^{11}C]PiB uptake in (a) cerebral cortex, (b) hippocampus and (c) thalamus. The AD animals showed earlier onset and more rapid progression of Aβ plaque deposition compared to WT animals at the age of 5 months. Meanwhile, significantly more [^{11}C]PiB uptake was found in the cerebral cortex, hippocampus and thalamus with Aβ plaques in AD mice as compared to WT mice at the age of 6 months. The symbol * * and * indicate significantly different means ($P < 0.01$ and $P < 0.05$, Kruskal-Wallis test, respectively) compared with the WT group. Data are presented as the mean ± SD. $n = 6$ for each group.

Note 16. Novel object recognition (NOR) test

Recognition memory in animals was assessed using the the novel object recognition (NOR) task. The NOR tests were carried out on WT and 3 × TgAD mice at 4 to 6 months of age. The analysis was performed over the course of three days with separation into the habituation day, training day and testing day. These trials were performed in a Plexiglas open-field box (50 cm × 50 cm × 50 cm) with black vertical walls and a floor. Before the NOR test each day, animals were placed in the Plexiglas testing box for 10 min, and the testing field was set up. The objects to be discriminated were silver-made and cone-shaped with 15 cm high. Mice were habituated to the open field for 1 h (habituation day). On training day, each mouse was placed in the open field and allowed to explore two identical objects for 10 min before being returned to their housing facility. On the testing day, animals received the NOR test for 3 h after the training day. One familiar object and one novel object were placed in the same location as on the training day.

The time spent exploring each object and the total amount of time spent exploring both objects were recorded. Exploration of an object was defined as orienting their noses toward the object, touching or sniffing at a distance smaller than 2 cm from each object, or when the animal's head was oriented within 45° of the object. Here, we applied a measure of cognitive function through the Preference Index (%). This is a ratio of the amount of time spent exploring the novel one on the test day over the total time spent exploring both objects, $N/(N+F) \times 100$ %, where N = time with the novel object, F = time with the familiar object. The index ranges from 0% to 100%, with greater than 50% indicating novel object preference, below 50% representing familiar object preference, and 50% indicating no preference [2,3].

NOR was tested every few months within the mice, dependent on their performance and focused in

around the age of 4 to 6 months. There was a slight and maintained decrease in the preference index in the AD group compared with that in the WT group as shown in **Figure S17**. The WT group overall still maintained a preference for the NOR through the ages of 4 to 6 months.

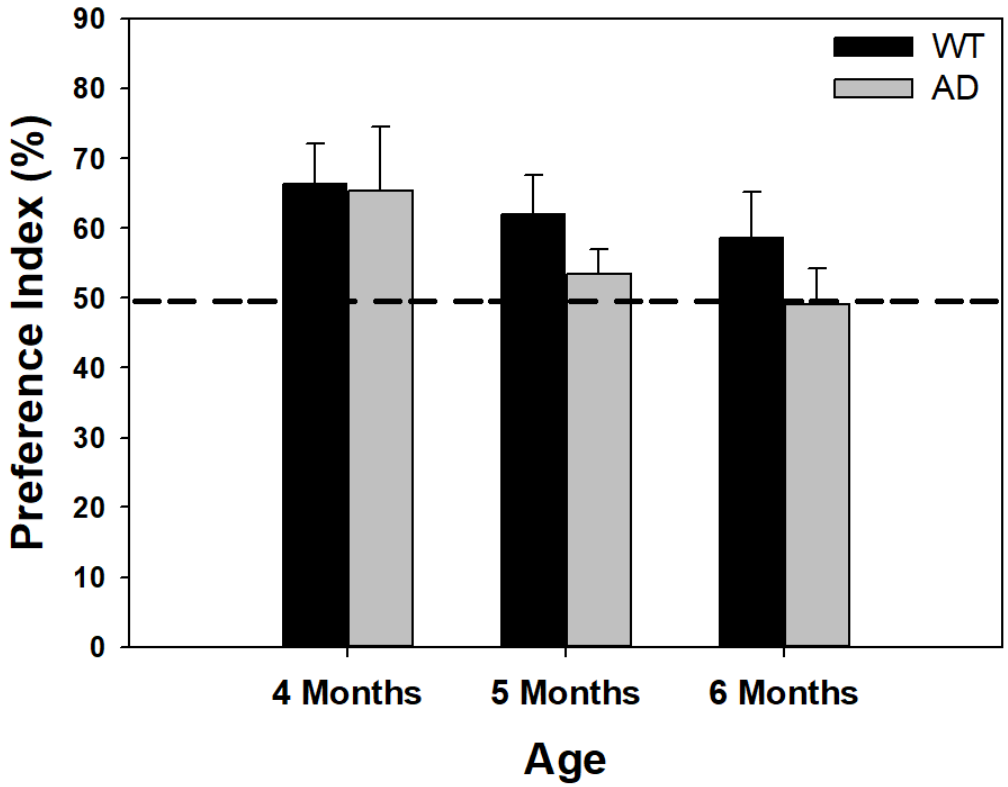

Figure S17. Overview of NOR results in WT and AD mice (4 to 6 months in age, $n = 6$ for each group).

Reference

1. Arendash GW, Gordon MN, Diamond DM, Austin LA, Hatcher JM, Jantzen P, DiCarlo G, Wilcock D, Morgan D. Behavioral assessment of Alzheimer's transgenic mice following long-term Abeta vaccination: task specificity and correlations between Abeta deposition and spatial memory. DNA Cell Biol. 2001; 20: 737-44.
2. Hammond RS, Tull LE, Stackman RW. On the delay-dependent involvement of the hippocampus in object recognition memory. Neurobiol Learn Mem. 2004; 82: 26–34.
3. Zhang R, Xue GZ, Wang SD, Zhang LH, Shi CJ, Xie X, Novel object recognition as a facile behavior test for evaluating drug effects in AβPP/PS1 Alzheimer's disease mouse model. J Alzheimers Dis. 2012; 31: 801–12.